1 # Fully automated, sequential focused ion beam milling

2 # for cryo-electron tomography

3

4 **Authors**

5 [1]Tobias Zachs, [1]João M. Medeiros, [2]Andreas Schertel, [1]Gregor L. Weiss, [1,3]Jannik
6 Hugener, [*1]Martin Pilhofer

7

8

9 **Affiliations**

10 [1]Institute of Molecular Biology & Biophysics, Eidgenössische Technische Hochschule
11 Zürich, CH-8093 Zürich, Switzerland

12 [2]Carl Zeiss Microscopy GmbH, Zeiss Customer Center Europe, D-73447 Oberkochen,
13 Germany

14 [3]Institute of Biochemistry, Eidgenössische Technische Hochschule Zürich, CH-8093
15 Zürich, Switzerland

16

17 [*]correspondence to: pilhofer@biol.ethz.ch

18

19

20

21

Abstract

Cryo-electron tomography (cryoET) has become a powerful technique at the interface of structural biology and cell biology, with the unique ability to determine structures of macromolecular complexes in their cellular context. A major limitation of cryoET is its restriction to relatively thin samples. Sample thinning by cryo-focused ion beam (cryoFIB) milling has significantly expanded the range of samples that can be analyzed by cryoET. Unfortunately, cryoFIB milling is low-throughput, time-consuming and manual. Here we report a method for fully automated sequential cryoFIB preparation of high-quality lamellae, including rough milling and polishing. We reproducibly applied this method to eukaryotic and bacterial model organisms, and show that the resulting lamellae are suitable for cryoET imaging and subtomogram averaging. Since our method reduces the time required for lamella preparation and minimizes the need for user input, we envision the technique will render previously inaccessible projects feasible.

Introduction

Cryo-electron tomography (cryoET) is a powerful imaging technique at the interface of cell biology and structural biology, able to image cells in a near-native state and determine the structure of macromolecular machines in their cellular context (Beck and Baumeister, 2016; Koning et al., 2018; Kooger et al., 2018; Oikonomou and Jensen, 2017; Plitzko et al., 2017). CryoET is restricted to samples that are well below 800 nm in thickness and therefore requires sample thinning techniques for specimens like mammalian cells, *C. elegans*, yeast, cyanobacteria, or biofilms. Biological cryoFIB milling is an emerging sample thinning technique, which uses a Gallium ion beam to ablate segments of the sample in order to generate thin lamellae that can be imaged by cryoET (Marko et al., 2007; Rigort et al., 2010). Unlike previous methodologies, cryoFIB milling produces artifact-free specimens, in which *in situ* structural information is preserved. Its application has led to important insights into mechanisms of cellular function (Albert et al., 2017; Böck et al., 2017; Bykov et al., 2017; Cai et al., 2018; Chaikeeratisak et al., 2019; Delarue et al., 2018; Khanna et al., 2019; Mahamid et al., 2016; Rast et al., 2019; Swulius et al., 2018; Weiss et al., 2019). Unfortunately, however, cryoFIB milling for cryoET is at an early stage of technical maturation and the available techniques are highly manual procedures with relatively low throughput.

In current lamella preparation workflows (Marko et al., 2007; Medeiros et al., 2018; Rigort et al., 2010; Strunk et al., 2012; Zhang et al., 2016), samples are vitrified on transmission electron microscopy (TEM) grids by plunge-freezing. Grids are then transferred to a FIB-scanning electron microscope (SEM) instrument, where potential targets are then identified by SEM and FIB imaging (Supplementary Fig. 1a/b). Using a series of 'rough milling' steps, sections above and below the desired lamella are sequentially removed by decreasing the separation between two milling areas and using decreasing FIB milling currents (700 to 100 pA) (Supplementary Fig. 1c-e). Once the lamella is thinned to ~500 nm, additional targets are identified and thinned by rough milling in a similar manner. To generate lamellae with a final thickness of 100-250 nm, the user returns to each target location and further thins ('polishes') each lamella using a low ($\leq$50 pA) current (Supplementary Fig. 1f).

This methodology allows the production of up to 16 lamellae in 10 h (Medeiros et al., 2018), however, during such a session, the process requires constant attention from the

3

67   operator. The milling process has to be monitored and manual user input is required every
68   10-15 min, e.g. to execute a series of repetitive tasks such as target identification,
69   positioning milling patterns, changing FIB currents, and visually determining milling end
70   points. This results in a strenuous procedure with a low throughput relative to the time
71   invested by the user, as well as significant idle times due to delays in input from the
72   operator. To overcome these issues, automated sequential cryoFIB milling has become of
73   paramount interest for the field.

74   **Setup of an automated milling session**

75   Here we report, to our knowledge, the first automated sequential FIB milling method for
76   the preparation of lamellae for subsequent cryoET imaging. Automation was
77   implemented on the Zeiss Crossbeam 550 FIB-SEM instrument, using routines that are
78   available in the SmartFIB software package (Zeiss Microscopy GmbH, Oberkochen,
79   Germany). Particularly important are the modules for stage backlash and drift correction,
80   which are critical for reliable targeting of lamella preparation sites. This allows the user
81   to set up all milling targets and then execute milling in an unattended, fully automated
82   manner.

83   To begin an automated milling session, FIB current alignments are verified to ensure
84   accurate milling (Fig. 1a). Grids are then loaded into the FIB-SEM instrument. To
85   simplify navigation and target identification, an SEM grid overview image is captured
86   and linked to the stage coordinates as described in the methods. Using the overview image
87   for stage navigation, the first milling site is identified and centered in both the SEM and
88   FIB views (Fig. 1b). To improve the accuracy of mechanical stage movements, the stage
89   is backlash-corrected when moved during automation. To ensure accurate targeting of the
90   milling site, a series of operations is executed before saving the final target position (Fig.
91   1c). First, stage backlash correction is manually executed and the target is re-centered in
92   the FIB image. Second, the target's stage coordinates are saved to the stage navigation
93   menu. Third, the stage is manually moved off-target and automatically returned to the
94   saved target location (Fig. 1d). In case the target is *not* properly centered, the above three
95   steps are repeated (Fig. 1e), otherwise the user can proceed.

96   Next, patterns with specific currents for rough milling (e.g. 700, 300 and 100 pA) and
97   polishing (e.g. 50 pA) are manually placed onto the FIB image of the target (Fig. 1f/f').

98   This is achieved by either generating a new set of patterns or by loading previously

99   designed patterns, which is faster and results in more uniform lamellae. To further

100   improve the accuracy of targeting, we incorporated an additional targeting step based on

101   drift correction (Fig. 1f/f'). To implement, each set of milling patterns receives a drift

102   correction box, with user-defined dimensions, which is manually placed in a location

103   close to the target. By capturing and saving an image of the drift correction box, the

104   milling patterns are anchored to their positions on the target.

105   After saving the first target to the queue, further targets are added by repeating the

106   described procedure. This setup-procedure takes ~9 min per target.

107   **Processes during automated milling session**

108   To begin sequential automation, exposure of the rough milling patterns that are saved in

109   the queue is started (Fig. 1g). For each target, the stage automatically moves to the target

110   position and executes stage backlash correction. Next, image shifts are determined

111   between the drift correction image that was recorded during the setup procedure and a

112   drift correction image that is recorded after arriving at the target location. Any existing

113   shifts are compensated for, using FIB beam shifts, to improve the precision of milling.

114   The rough milling patterns are then exposed, from the highest to the lowest current

115   strength. Previously, manual milling methods used a real-time view in order to determine

116   the time that the FIB needs to cut through the specimen. In our automated approach, the

117   exposure time is calculated by the software using a user-specified milling depth (typically

118   10 µm), milling current, pattern size and material type (e.g. vitrified ice). After exposing

119   the rough milling patterns for the first target, the procedure is automatically repeated for

120   the remaining targets.

121   Subsequently, the user can decide whether to perform polishing for all targets in a manual

122   or automated manner (Fig. 1h). The automation of polishing follows the routine described

123   above.

124

125

126

5

Application of sequential automated milling

During the development of this method, we tested automated sequential milling using the model organisms *S. cerevisiae* strain SK1 (hereafter yeast) and the multicellular cyanobacteria *Anabaena* sp. PCC 7120 (hereafter *Anabaena*) in six independent milling sessions (Table 1). The number of attempted lamellae per session ranged from five to 20 (Fig. 2). Rough milling success, as defined by the presence of a lamella at the targeted location after rough milling, was 99% (n=73). The only failure in lamella production was the result of a user error, as rough milling was accidentally executed on the same target twice (session F). In session B.1 and B.2, lamellae were successfully generated on ten targets that were spread across two grids containing two different samples (Table 1). This shows the robustness of the targeting routine despite sample variations and the execution of large stage movements during automation.

While these results present a significant step forward, we next set out to implement automated sequential lamella polishing. In a series of sessions (B.2-F), we milled between five and 20 targets. In total, the success rate (intact lamella detected after polishing) of automated sequential polishing was 81% (n=57 rough lamellae). Importantly, 9 of the 11 failed polishing attempts occurred in session C, in which the rough-milled lamellae were left in the FIB-SEM instrument for 10 h before automated polishing was started. Prior to polishing, these rough lamellae showed signs of bending, which likely resulted in failure in lamellae polishing. Sequential automated lamella polishing should therefore be executed without delay after rough milling. Other reasons for failure in lamella milling could include sample heterogeneity and errors in targeting. If, however, session C were not taken into account, this automated sequential FIB milling methodology would have a 95% (n=37) success rate.

Assessment of sample quality

In order to assess sample quality, we transferred the grids from all sessions to the cryoTEM. Of the lamellae that were generated in a fully automated manner, 11% (n=46) were lost in transfer. All remaining lamellae could be imaged by cryoET. From the cryotomograms, we determined the lamellae thicknesses to range from 155 to 379 nm (average 232 nm; final polishing patterns were spaced 300 nm apart) (Supplementary Fig.

6

157 2). Lamellae that were manually polished (sessions A/B.1) had a comparable average
158 thickness of 258 nm (final polishing patterns were spaced 300 nm apart).

159 CryoET imaging of the automatically generated lamellae revealed distinct cellular
160 features and macromolecular complexes. Yeast tomograms showed a characteristic
161 nucleoplasm, cytoplasmic ribosomes, nuclear envelope, nuclear pore complexes, and
162 cellular compartments (Fig. 3b). *Anabaena* tomograms showed thylakoid membranes,
163 phycobilisomes and septal junctions (Fig. 3c). To further assess sample and data quality,
164 we performed subtomogram averaging of *Anabaena* septal junctions, which had been
165 characterized recently by a manual cryoFIB milling/cryoET approach (Weiss et al.,
166 2019). From nine lamellae, a total of 412 subvolumes were extracted, averaged and
167 classified in order to remove misaligned particles. The 343 remaining subvolumes were
168 then averaged and symmetrized. The resulting structure revealed key features, including
169 a cap module with five arches, a plug module and a tube module (Fig. 3e-h). Fourier shell
170 correlation (FSC) analyses indicate that the average has a resolution that is similar to a
171 structure that was calculated using the same number of particles extracted from
172 tomograms generated in a previous study (Weiss et al., 2019) (manual milling)
173 (Supplementary Fig. 3).

174 **Discussion**

175 In conclusion, our automated sequential cryoFIB milling method allows for the
176 production of high-quality lamellae for cryoET imaging and will impact cryoFIB/cryoET
177 projects in several ways. First, the time investment by the operator is significantly reduced
178 from ~10 h in a manual milling session to ~2.4 h for an automated sequential milling
179 session, assuming 16 targets are milled. Second, by removing the need for frequent user
180 inputs and idle times, the minimum required machine time is reduced from ~38 min
181 (Medeiros et al., 2018) (i.e. 16 lamellae in 10 h) to ~25.5 min (9 min setup plus 16.5 min
182 milling) per lamella. Third, based on the robustness and customizable nature of the
183 method, the procedure can be adapted to a wide range of samples and milling techniques
184 (Toro-Nahuelpan et al.; Wolff et al., 2019). Fourth, the automated procedure will allow
185 the user to systematically explore novel milling methods by reusing uniform milling
186 patterns. Fifth, the method can generally be combined with correlated approaches that
187 allow for target pre-screening, for instance cryo-light microscopy or cryo-FIB-SEM
188 volume imaging (Eibauer et al., 2012; Gorelick et al., 2019; Koning et al., 2014; Schertel

7

189   et al., 2013; Schorb et al., 2017; Sviben et al., 2016; Vidavsky et al., 2016). That said, the

190   higher throughput achieved by automated cryoFIB milling (shown here) in combination

191   with fast cryoET data collection schemes (Chreifi et al., 2019; Eisenstein et al., 2019),

192   might in many cases eliminate the need for target pre-identification by correlated

193   approaches. Altogether, the development of automated sequential cryoFIB milling

194   renders cryoET applicable to previously unfeasible projects.

195

196   **Acknowledgments**

202

8

Methods

Overview of the equipment and workflow

The method was established and tested on a Crossbeam 550 FIB-SEM instrument (Carl Zeiss Microscopy) equipped with a copper band-cooled mechanical cryo-stage and an integrated VCT500 vacuum transfer system (Leica Microsystems). The detectors used included an InLens secondary elelctron (SE) detector for determining grid topology (Carl Zeiss Microscopy) and a SE2 detector for identifying milling targets and assessing the ice thickness (Carl Zeiss Microscopy). In our workflow, EM grids were prepared with budding yeast strain SK1 and *Anabaena* sp. PCC 7120, and clipped into FIB milling Autogrids (ThermoFisher Scientific, Waltham, Massachusetts, U.S.). These grids were then mounted onto a pre-tilted Autogrid holder (Medeiros et al., 2018) (Leica Microsystems) using a VCM loading station (Leica Microsystems). Using the VCT500 shuttle, the Autogrid holder was transferred to an ACE600 cryo-sputter coater (Leica Microsystems) under cryogenic conditions and the samples were sputter-coated with a 4 nm thick layer of tungsten. After sputter coating, the samples were transferred into the Crossbeam 550 using the VCT500 shuttle. In the Crossbeam 550, the gas injection system (UniGIS) was used to deposit an organometallic platinum precursor layer onto each grid. Automated sequential FIB milling was subsequently set up and executed. Sample preparation, plunge-freezing, Autogrid mounting, holder loading and vacuum cryo-transfer steps were executed similarly to what was described in Medeiros et al. 2018. Any deviations to the previously published protocol are described below.

Cell culture and plunge freezing

FIB milling tests were performed using the cyanobacterial strain *Anabaena* sp. PCC 7120 and the *S. cerevisiae* strain SK1. The *Anabaena* strain was grown and prepared for FIB milling as previously described in Weiss et al. 2019. Yeast cells were prepared as previously described by Medeiros et al. 2018.

Equipment calibration

To ensure that automated sequential FIB milling was successful, the Crossbeam 550 was properly aligned. While the SEM column alignments are stable and non-essential during automated milling, the FIB alignment between different currents at a given voltage (30

9

233   kV for biological cryo-samples) should be checked and optimized. Typically, this
234   calibration is done weekly or when deemed necessary and takes roughly 60 min to
235   complete. In case of deviation, on-the-fly adjustments are possible on a loaded cryo-
236   sample, however, standard calibration procedures are best performed on a silicon wafer
237   due to its structural homogeneity, which allows better evaluation of the FIB beam shape.
238   Once inserted into the chamber, the stage was tilted by 54º to be perpendicular to the FIB
239   beam and then moved to the working distance (i.e. coincidence point). Using the 'spot'
240   function in an unexposed sample region, the beam was focused to its spot size allowing
241   it to burn a hole into the silicon. If the current is properly calibrated, then the beam will
242   produce a spot that is round with sharp edges. This was best seen when using a mixed
243   signal of the InLens and SE2 detector. If a beam spot had imperfections, like a tailing
244   edge, beam parameters including focus, stigmatism and aperture alignments need to be
245   improved and saved. After optimizing these parameters for each current, all currents were
246   aligned against the reference current. This was best performed by centering an easily
247   recognizable structure like a burnt hole for each beam onto the exact position in the image
248   taken with the reference current. Finally, to ensure that the currents were properly aligned,
249   a location is imaged by each current. If properly aligned, switching between currents
250   should not lead to focus changes or beam offsets.

251   Sample coating

252   To enhance sample conductivity and decrease the effects of charging, EM grids were
253   coated with a ~4 nm layer of tungsten using the sputter coating head on the ACE600.
254   After inserting the holder into the FIB-SEM, a protection layer of organometallic
255   platinum precursor was deposited onto each grid to minimize the curtaining effect. For
256   cold deposition of platinum precursor, the holder was moved 3 mm below the coincidence
257   point and was tilted to 20 degrees. By positioning the gas injection system (GIS) needle
258   above each grid and opening the GIS for 30 s, a layer of platinum precursor was deposited
259   onto the sample. Since the GIS needle was mounted at a similar angle as the FIB column,
260   deposition of platinum occurred preferentially on the side of the cells where the FIB beam
261   hits the sample, ensuring the best protection. For deposition under cryo-conditions, it is
262   essential that the heating element of the GIS needle and reservoir are turned off to keep
263   the system at room temperature (28 °C).

264

265 Stage registration

266 To assist in the identification of targets, overview images of an entire EM grid are taken.

267 On the Zeiss Crossbeam 550, these images can be coupled to the stage navigation. To

268 calibrate stage registration a high-resolution (4096 x 3072 pixels, 35x) overview image

269 was taken with the SE2 detector, which provided the best information for identifying

270 targets inside the vitrified ice and determining ice thickness. This overview image was

271 then loaded onto the stage navigation bar and registered by correlating three distinctive

272 points on the image to their specific positions on the stage as observed in the live SEM

273 view. After completion, double clicking on a desired target image location in the

274 navigation bar automatically moves the stage to the location of interest. In addition,

275 backlash correction was also included for all automated stage movements, using the user

276 preference settings of the software SmartSEM (Carl Zeiss Microscopy).

277 Defining milling materials

278 To permit unsupervised automation of lamellae production, the Crossbeam 550 was

279 calibrated to mill a cross-section with a specified depth through the sample. To ensure

280 proper milling, the system needs to be calibrated for a distinct 'material' so that the correct

281 milling parameters like dose are applied during milling. For cryo-TEM lamella

282 preparation the material "vitrified ice" was created using a dose calibration of 20 mC /

283 cm^2 being equivalent to a milling depth of 1 μm in cross-section mode.

284 Parameters for imaging and milling

285 For SEM imaging, voltages from 1.9 - 5 kV and a constant current of 28 pA were used.

286 To capture SEM images, we most commonly used the InLens detector to obtain surface

287 information of the sample. During FIB imaging, on the other hand, a fixed voltage of 30

288 kV and a low current (20pA) was used. FIB images were usually captured by using the

289 SE2 detector, which is less sensitive to imaging-induced charging. During automated

290 sequential milling, four sets of currents above and below the desired lamellae were used.

291 For rough milling 700 pA, 300 pA and 100 pA currents were implemented. To then polish

292 the lamellae, a 50 pA current was used. For milling, we defined the patterns to be executed

293 using bi-directional and cross-section cycle mode with a 10 μm milling depth.

294

295   Automated sequential FIB milling protocol

296   To generate high quality lamellae, it was essential to prepare the FIB-SEM and sample

297   for automated sequential milling. Preparations included checking and calibrating the FIB

298   currents, coating the sample with a layer of tungsten and organometallic platinum, and

299   performing stage registration. Once these steps were executed, automated sequential

300   milling was initiated by identifying and setting up milling targets.

301   The grid overview image in the stage navigator was used to identify a milling target. The

302   identified target was then manually centered in the live FIB view with the aid of the SEM.

303   To improve the accuracy of automated stage movements, backlash correction was

304   performed manually and implemented for all automated stage movements. The target's

305   stage coordinates were then saved in the stage navigator. To ensure that the instrument

306   was able to perform targeting during automation, the stage was manually moved away

307   from the target and then instructed to move back to its saved location. The target was

308   located using the live FIB view and if necessary, manually centered again. If manual

309   centering was required, the new stage location was saved and the instrument's ability to

310   perform targeting was tested again. To ensure successful milling during automation, it

311   was essential to refine the stage location until the stage was able to perform targeting

312   successfully.

313   Once an accurate stage movement was achieved, milling patterns were placed onto a

314   target FIB image captured using SmartFIB. In SmartFIB, each pattern contains specific

315   milling conditions (i.e. current, milling depth, size, shape, etc.) and a designated FIB

316   milling location. SmartFIB allows the placing of multiple patterns with different

317   conditions onto a single FIB image in order to perform automated milling. Patterns were

318   placed and their properties were changed by using the SmartFIB GUI in the 'Attributes'

319   tab. When testing this methodology, we placed eight rectangular milling patterns: six

320   rough milling and two polishing patterns (Supplementary table 1). The final polishing

321   patterns were spaced 300 nm apart, which from our experience results in an average

322   lamella thickness of 225-275 nm. To make uniform lamellae it was also possible to save

323   these eight patterns as a recipe, which can be dragged and dropped onto images of other

324   milling targets. To then save these milling patterns, it was essential to separate the rough

325   and polishing patterns. This was accomplished by deleting the polishing patterns from

326   our recipe, saving only the rough milling patterns, undoing the deletion of the polishing

12

327   patterns (using the SmartFIB Undo button), deleting all rough milling patterns and then

328   saving only the polishing patterns.

329   To improve the targeting accuracy of this methodology, a drift correction step was also

330   added to each set of rough and polishing milling patterns immediately before being saved.

331   This was done in the SmartFIB 'attributes' tab, by capturing and saving an image of a

332   defined region of the FIB view. During the automated protocol SmartFIB would use this

333   image to perform image recognition before beginning milling and compensate for small

334   shifts to ensure the milling patterns are placed correctly on the target. When testing this

335   methodology, it was important to save and then load the same drift correction image for

336   both the rough and polishing milling patterns. This ensured the highest accuracy when

337   moving from rough milling to polishing.

338   After saving a set of rough and polishing patterns, the described method can be repeated

339   for further targets. For an automated protocol, about 9 min were needed to set up each

340   target. It is possible to also automate the milling of targets found on separate EM grids.

341   Once satisfied with the number of targets, all rough milling recipes in the SmartFIB queue

342   were selected and exposed. Exposure of a typical rough milling target takes about 12

343   min. Upon completion, rough milling targets were observed using the SEM and FIB to

344   determine their quality. To then initiate polishing, it is possible to either tick all polishing

345   recipes and expose them, or individually move to each target using SmartFIB, take a FIB

346   image, manually drag polishing patterns into place and expose the lamella. Polishing

347   typically took about 4.5 min. Once all targets are polished, the lamellae are removed from

348   the instrument and stored. It is essential to note that we aimed to keep the lamellae in the

349   instrument for <2 h after beginning polishing to minimize contamination. In theory, this

350   limits our lamellae production to ≤20 targets. If, however, aspects including the milling

351   depth, pattern sizes or currents were changed, it would be possible to generate more

352   lamellae. Note that in our attempts, grids with milled lamellae were transported in a dry-

353   shipper from Zeiss Oberkochen, Germany to Zürich, Switzerland prior to cryoET

354   imaging, possibly resulting in some lamellae breaking. An overview of all the milling

355   attempts performed can be found in Table 1.

356   Cryo-electron tomography, tomogram reconstruction and subtomogram averaging

357   Data was collected on a Titan Krios 300kV electron microscope (ThermoFisher)

358   equipped with a field emission gun, imaging filter (Gatan, Munich, Germany) (slit width

13

359 20 eV) and K2 Summit direct electron detector (Gatan). To generate an overview of each

360 grid, grid montages were collected at 135x magnification using SerialEM (Mastronarde,

361 2005). UCSF Tomo (Zheng et al., 2007) was used for automated recording of tilt series

362 (+60° and -60° tilt range, 2° increments). Data was collected at a defocus of -8 μm, total

363 accumulated dose of ~140 e$^-$ / Å^2 and pixel size of 3.38 Å. Tomogram reconstruction and

364 subtomogram averaging was performed according to Weiss et al. 2019. Briefly,

365 tomograms were reconstructed using the IMOD package (Kremer et al., 1996) and

366 subtomogram averaging was performed using PEET (Nicastro et al., 2006). A total of 412

367 particles were extracted and averaged in a box of 44 x 44 x 44 pixels with a pixel size of

368 0.68 nm. PEET classification was then used to remove misaligned particles (343 final

369 particles). 5-fold symmetry was applied to obtain the final average. The FSC (Fourier

370 Shell Correlation) was generated by using the PEET command calcFSC.

371 Data and code availability

372 Example tomograms of yeast and *Anabaena* lamellae milled in a fully automated manner

373 and the final septal junction subtomogram average determined in this study were

374 deposited to the Electron Microscopy Data Bank (accession number EMDB xxx-yyy for

375 the tomograms and zzz for the subtomogram average).

376

References

Albert S, Schaffer M, Beck F, Mosalaganti S, Asano S, Thomas HF, Plitzko JM, Beck M, Baumeister W, Engel BD. 2017. Proteasomes tether to two distinct sites at the nuclear pore complex. *Proc Natl Acad Sci U S A* **114**:13726–13731. doi:10.1073/pnas.1716305114

Beck M, Baumeister W. 2016. Cryo-Electron Tomography: Can it Reveal the Molecular Sociology of Cells in Atomic Detail? *Trends Cell Biol* **26**:825–837. doi:10.1016/J.TCB.2016.08.006

Böck D, Medeiros JM, Tsao H-F, Penz T, Weiss GL, Aistleitner K, Horn M, Pilhofer M. 2017. In situ architecture, function, and evolution of a contractile injection system. *Science* **357**:713–717. doi:10.1126/science.aan7904

Bykov YS, Schaffer M, Dodonova SO, Albert S, Plitzko JM, Baumeister W, Engel BD, Briggs JA. 2017. The structure of the COPI coat determined within the cell. *Elife* **6**. doi:10.7554/eLife.32493

Cai S, Böck D, Pilhofer M, Gan L. 2018. The in situ structures of mono-, di-, and trinucleosomes in human heterochromatin. *Mol Biol Cell* **29**:2450–2457. doi:10.1091/mbc.E18-05-0331

Chaikeeratisak V, Khanna K, Nguyen KT, Sugie J, Egan ME, Erb ML, Vavilina A, Nonejuie P, Nieweglowska E, Pogliano K, Agard DA, Villa E, Pogliano J. 2019. Viral Capsid Trafficking along Treadmilling Tubulin Filaments in Bacteria. *Cell* **177**:1771-1780.e12. doi:10.1016/J.CELL.2019.05.032

Chreifi G, Chen S, Metskas LA, Kaplan M, Jensen GJ. 2019. Rapid tilt-series acquisition for electron cryotomography. *J Struct Biol* **205**:163–169. doi:10.1016/J.JSB.2018.12.008

Delarue M, Brittingham GP, Pfeffer S, Surovtsev IV, Pinglay S, Kennedy KJ, Schaffer M, Gutierrez JI, Sang D, Poterewicz G, Chung JK, Plitzko JM, Groves JT, Jacobs-Wagner C, Engel BD, Holt LJ. 2018. mTORC1 Controls Phase Separation and the Biophysical Properties of the Cytoplasm by Tuning Crowding. *Cell* **174**:338-349.e20. doi:10.1016/J.CELL.2018.05.042

15

406   Eibauer M, Hoffmann C, Plitzko JM, Baumeister W, Nickell S, Engelhardt H. 2012.
407   Unraveling the structure of membrane proteins in situ by transfer function corrected
408   cryo-electron tomography. *J Struct Biol* **180**:488–496.
409   doi:10.1016/J.JSB.2012.09.008

410   Eisenstein F, Danev R, Pilhofer M. 2019. Improved applicability and robustness of fast
411   cryo-electron tomography data acquisition. *J Struct Biol*.
412   doi:10.1016/J.JSB.2019.08.006

413   Gorelick S, Buckley G, Gervinskas G, Johnson TK, Handley A, Caggiano MP,
414   Whisstock JC, Pocock R, de Marco A. 2019. PIE-scope, integrated cryo-correlative
415   light and FIB/SEM microscopy. *Elife* **8**. doi:10.7554/eLife.45919

416   Khanna K, Lopez-Garrido J, Zhao Z, Watanabe R, Yuan Y, Sugie J, Pogliano K, Villa
417   E. 2019. The molecular architecture of engulfment during Bacillus subtilis
418   sporulation. *Elife* **8**. doi:10.7554/eLife.45257

419   Koning RI, Celler K, Willemse J, Bos E, van Wezel GP, Koster AJ. 2014. Correlative
420   Cryo-Fluorescence Light Microscopy and Cryo-Electron Tomography of
421   Streptomyces. *Methods Cell Biol* **124**:217–239. doi:10.1016/B978-0-12-801075-
422   4.00010-0

423   Koning RI, Koster AJ, Sharp TH. 2018. Advances in cryo-electron tomography for
424   biology and medicine. *Ann Anat - Anat Anzeiger* **217**:82–96.
425   doi:10.1016/J.AANAT.2018.02.004

426   Kooger R, Szwedziak P, Böck D, Pilhofer M. 2018. CryoEM of bacterial secretion
427   systems. *Curr Opin Struct Biol* **52**:64–70. doi:10.1016/J.SBI.2018.08.007

428   Kremer JR, Mastronarde DN, McIntosh JR. 1996. Computer Visualization of Three-
429   Dimensional Image Data Using IMOD. *J Struct Biol* **116**:71–76.
430   doi:10.1006/JSBI.1996.0013

431   Mahamid J, Pfeffer S, Schaffer M, Villa E, Danev R, Cuellar LK, Förster F, Hyman AA,
432   Plitzko JM, Baumeister W. 2016. Visualizing the molecular sociology at the HeLa
433   cell nuclear periphery. *Science* **351**:969–72. doi:10.1126/science.aad8857

434   Marko M, Hsieh C, Schalek R, Frank J, Mannella C. 2007. Focused-ion-beam thinning
435   of frozen-hydrated biological specimens for cryo-electron microscopy. *Nat*
436   *Methods* **4**:215–217. doi:10.1038/nmeth1014

437   Mastronarde DN. 2005. Automated electron microscope tomography using robust
438   prediction of specimen movements. *J Struct Biol* **152**:36–51.
439   doi:10.1016/J.JSB.2005.07.007

440   Medeiros JM, Böck D, Weiss GL, Kooger R, Wepf RA, Pilhofer M. 2018. Robust
441   workflow and instrumentation for cryo-focused ion beam milling of samples for
442   electron cryotomography. *Ultramicroscopy* **190**:1–11.
443   doi:10.1016/J.ULTRAMIC.2018.04.002

444   Nicastro D, Schwartz C, Pierson J, Gaudette R, Porter ME, McIntosh JR. 2006. The
445   molecular architecture of axonemes revealed by cryoelectron tomography. *Science*
446   **313**:944–8. doi:10.1126/science.1128618

447   Oikonomou CM, Jensen GJ. 2017. Cellular Electron Cryotomography: Toward
448   Structural Biology In Situ. *Annu Rev Biochem* **86**:873–896. doi:10.1146/annurev-
449   biochem-061516-044741

450   Plitzko JM, Schuler B, Selenko P. 2017. Structural Biology outside the box — inside the
451   cell. *Curr Opin Struct Biol* **46**:110–121. doi:10.1016/J.SBI.2017.06.007

452   Rast A, Schaffer M, Albert S, Wan W, Pfeffer S, Beck F, Plitzko JM, Nickelsen J, Engel
453   BD. 2019. Biogenic regions of cyanobacterial thylakoids form contact sites with
454   the plasma membrane. *Nat Plants* **5**:436–446. doi:10.1038/s41477-019-0399-7

455   Rigort A, Bäuerlein FJB, Leis A, Gruska M, Hoffmann C, Laugks T, Böhm U, Eibauer
456   M, Gnaegi H, Plitzko JM. 2010. Micromachining tools and correlative approaches
457   for cellular cryo-electron tomography. *J Struct Biol* **172**:169–179.
458   doi:10.1016/J.JSB.2010.02.011

459   Schertel A, Snaidero N, Han H-M, Ruhwedel T, Laue M, Grabenbauer M, Möbius W.
460   2013. Cryo FIB-SEM: Volume imaging of cellular ultrastructure in native frozen
461   specimens. *J Struct Biol* **184**:355–360. doi:10.1016/J.JSB.2013.09.024

462 Schorb M, Gaechter L, Avinoam O, Sieckmann F, Clarke M, Bebeacua C, Bykov YS,

463   Sonnen AF-P, Lihl R, Briggs JAG. 2017. New hardware and workflows for semi-

464   automated correlative cryo-fluorescence and cryo-electron

465   microscopy/tomography. *J Struct Biol* **197**:83–93. doi:10.1016/J.JSB.2016.06.020

466 Strunk KM, Ke D, Gray JL, Zhang P. 2012. Thinning of Large Biological Cells for

467   Cryo-TEM Characterization by Cryo-FIB Milling. *J Microsc* **247**:220.

468   doi:10.1111/J.1365-2818.2012.03635.X

469 Sviben S, Gal A, Hood MA, Bertinetti L, Politi Y, Bennet M, Krishnamoorthy P,

470   Schertel A, Wirth R, Sorrentino A, Pereiro E, Faivre D, Scheffel A. 2016. A

471   vacuole-like compartment concentrates a disordered calcium phase in a key

472   coccolithophorid alga. *Nat Commun* **7**:11228. doi:10.1038/ncomms11228

473 Swulius MT, Nguyen LT, Ladinsky MS, Ortega DR, Aich S, Mishra M, Jensen GJ.

474   2018. Structure of the fission yeast actomyosin ring during constriction. *Proc Natl*

475   *Acad Sci U S A* **115**:E1455–E1464. doi:10.1073/pnas.1711218115

476 Toro-Nahuelpan M, Zagoriy I, Senger F, Blanchoin L, Théry M, Mahamid J. *BioRxiv*

477   Tailoring cryo-electron microscopy grids by photo-micropatterning for in-cell

478   structural studies. doi:10.1101/676189

479 Vidavsky N, Akiva A, Kaplan-Ashiri I, Rechav K, Addadi L, Weiner S, Schertel A.

480   2016. Cryo-FIB-SEM serial milling and block face imaging: Large volume

481   structural analysis of biological tissues preserved close to their native state. *J Struct*

482   *Biol* **196**:487–495. doi:10.1016/J.JSB.2016.09.016

483 Weiss GL, Kieninger A-K, Maldener I, Forchhammer K, Pilhofer M. 2019. Structure

484   and Function of a Bacterial Gap Junction Analog. *Cell* **178**:374–384.

485   doi:10.1016/j.cell.2019.05.055

486 Wolff G, Limpens RWAL, Zheng S, Snijder EJ, Agard DA, Koster AJ, Bárcena M.

487   2019. Mind the gap: micro-expansion joints drastically decrease the bending of

488   FIB-milled cryo-lamellae. *J Struct Biol*. doi:10.1016/J.JSB.2019.09.006

489 Zhang J, Ji G, Huang X, Xu W, Sun F. 2016. An improved cryo-FIB method for

490   fabrication of frozen hydrated lamella. *J Struct Biol* **194**:218–223.

491   doi:10.1016/J.JSB.2016.02.013

492   Zheng SQ, Keszthelyi B, Branlund E, Lyle JM, Braunfeld MB, Sedat JW, Agard DA.

493   2007. UCSF tomography: An integrated software suite for real-time electron

494   microscopic tomographic data collection, alignment, and reconstruction. *J Struct*

495   *Biol* **157**:138–147. doi:10.1016/j.jsb.2006.06.005
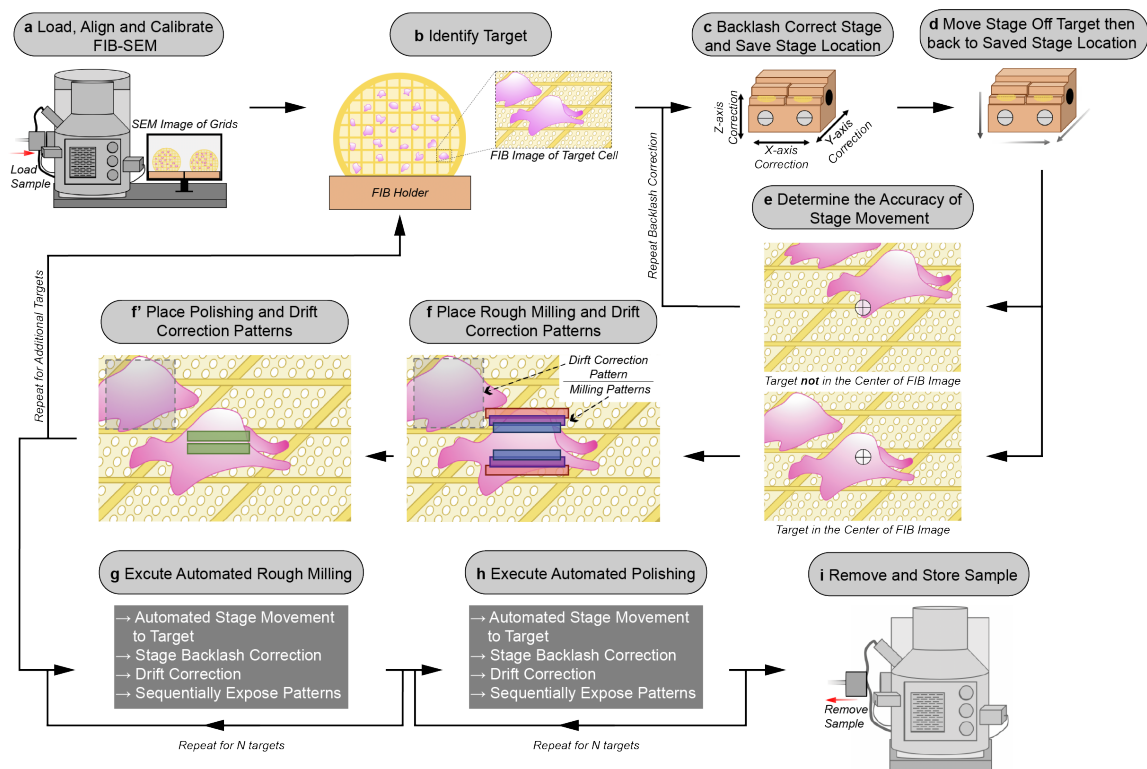
496

497

498

499

500

501

502

503

504 **Figure 1. Schematic of the automated sequential cryoFIB milling workflow.**

505 **a**: FIB currents are aligned and calibrated, and the sample is loaded into the FIB-SEM
506 instrument.

507 **b**: A target cell is identified on the grid with the FIB.

508 **c**: To correct for errors in mechanical stage movements, backlash correction of the stage
509 is performed. The resulting stage location is saved in the stage navigator.

510 **d**: The stage is randomly moved out of position by the user. Using the saved
511 coordinates, the stage is moved back to the target using the saved position in the stage
512 navigator.

513 **e**: The accuracy of this autonomous stage movement is determined by the user. If the
514 target is not centered in the FIB image, backlash correction is repeated until accurate
515 targeting is achieved (c-e).

516 **f/f'**: Rough milling, polishing and drift correction patterns are placed onto the image.
517 Rough milling and polishing patterns are saved separately to the queue. The procedure
518 (b-f') is repeated to select additional targets.

20

519   **g**/**h**: Rough milling and lamellae polishing are executed automatically.

520   **i**: The grids with milled lamellae are removed and stored.

521

522
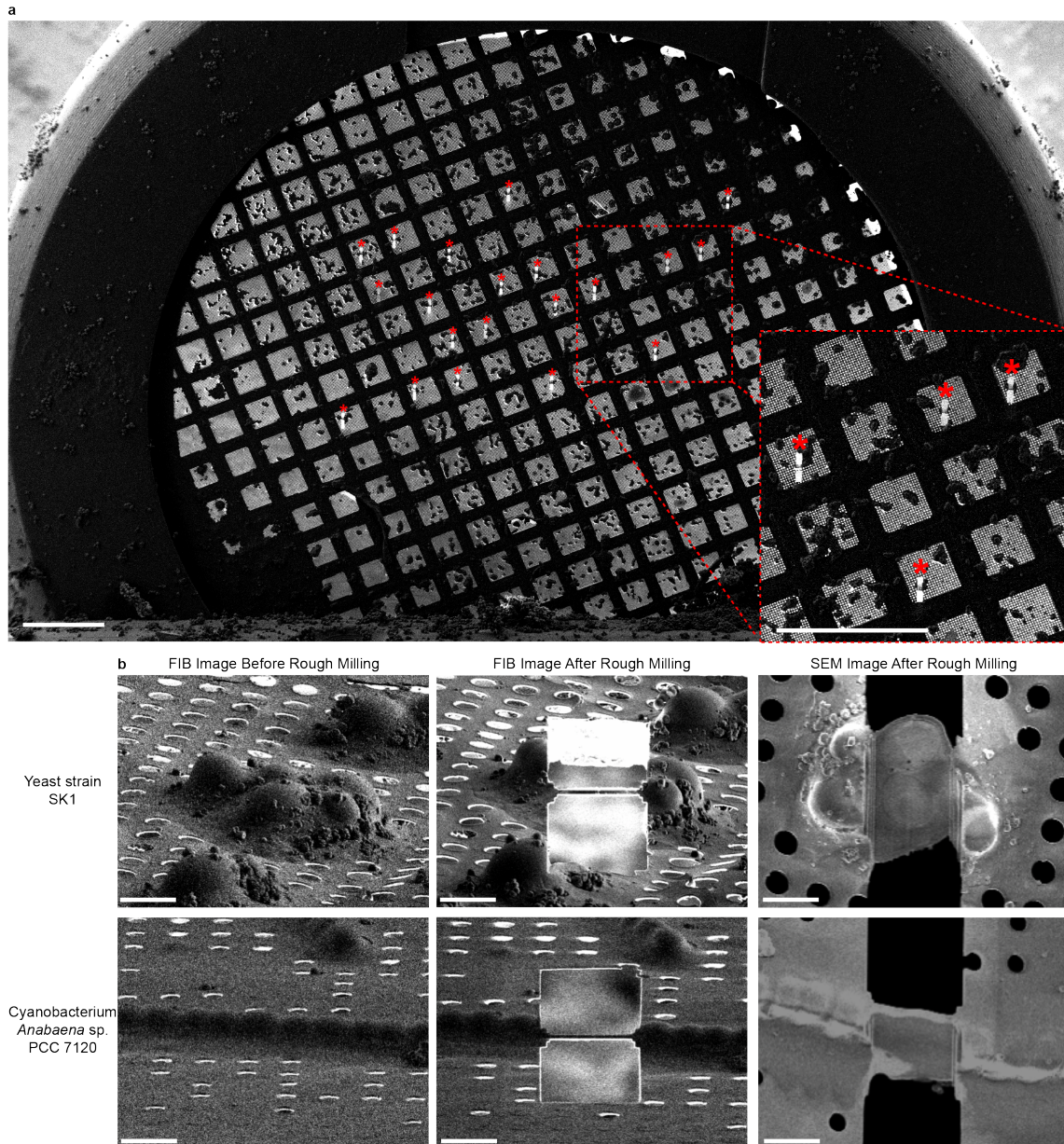
Figure 2. Representative images of lamellae generated by automated sequential rough milling.

a: SEM grid overview image including 20 yeast targets (asterisks) on which rough milling was performed in an automated sequential manner (session C). Bars, 200 µm.

b: Representative SEM and FIB images of yeast and cyanobacterial *Anabaena* cells captured before and after fully automated sequential rough milling (session B.1 and B.2). Bars, 5 µm.

532
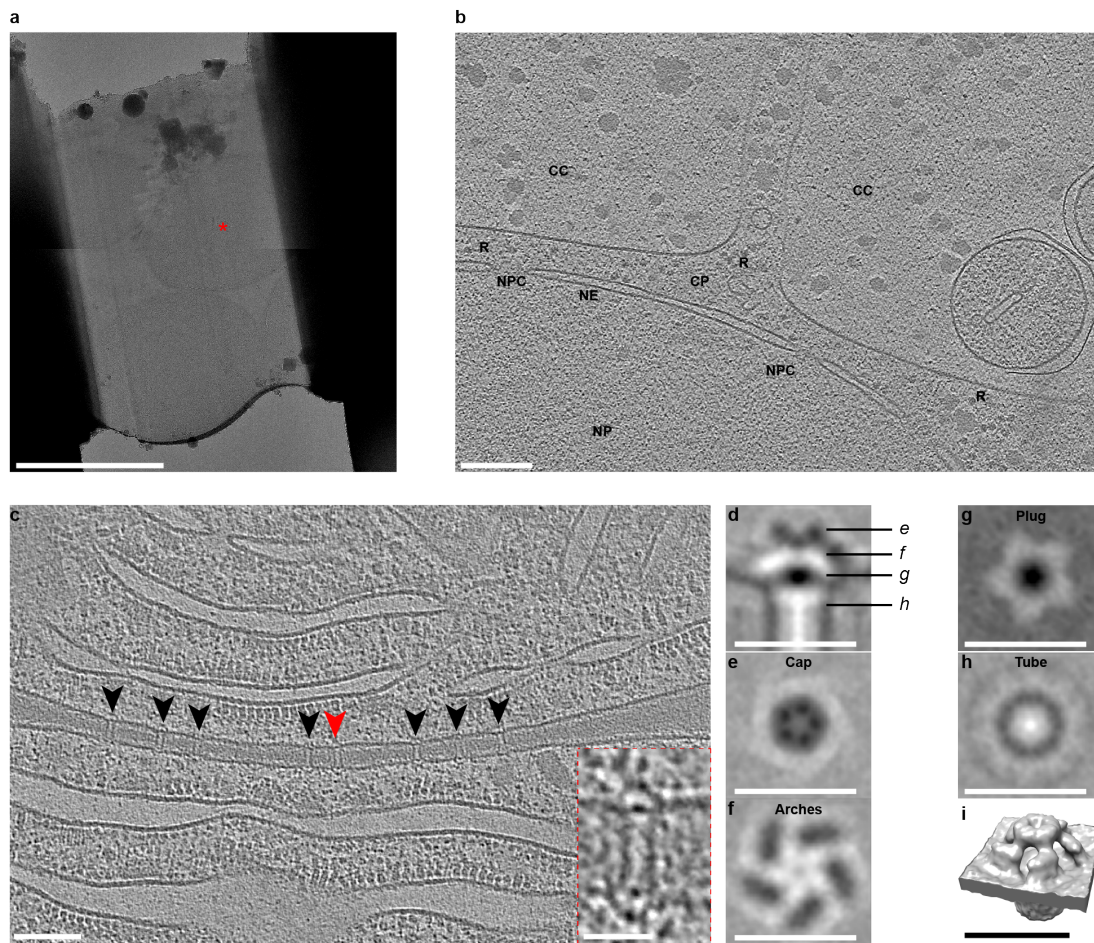
Figure 3. Automated sequential cryoFIB milling results in high-quality lamellae and cryotomograms.

a: CryoTEM overview image of a typical lamella (session C) containing multiple yeast cells. Red mark indicates the cell imaged in (b). Bar, 5 μm.

b: Shown is an 18 nm thick slice through a cryotomogram of a yeast cell (session C) [indicated by red mark in (a)]. The thickness of the lamella was determined to be 225 nm. The tomogram shows a characteristic nucleoplasm (NP), nuclear pore complexes (NPC), nuclear envelope (NE), cytoplasm (CP), cytoplasmic ribosomes (R), and other cellular compartments (CC). Bar, 200 nm.

c: Shown is a 14 nm thick slice through a cryotomogram of a septum between two *Anabaena* sp. PCC 7120 cyanobacteria cells (session F). The thickness of the lamella was determined to be 208 nm. Arrowheads indicate septal junctions. The inset shows a magnified view of the septal junction indicated by a red arrowhead. Other cellular features are cytoplasmic membranes (CM), phycobilisomes (PB), thylakoid membranes

23

547   (TM) and septal peptidoglycan (PG). Bars, 100 nm and 25 nm (inset).

548   **d-i**: A subtomogram average was generated by 5-fold symmetrizing 343 septal junctions

549   that were extracted from nine tomograms. Shown are longitudinal (d) and perpendicular

550   (e-h) slices (thickness 0.68 nm) and a surface rendering (i) of the symmetrized average.

551   The observed characteristic structural modules were similar to a recent study that

552   applied manual cryoFIB milling (Weiss et al., 2019) (also see Supplementary Fig. 3).

553   Bars, 25 nm.

554

555   **Table 1. Overview and success rates of milling sessions.**

Session	Sample Type	Rough Milling	Rough Milling Success	Polishing	Polishing Success	Comments
A	Cyanobacterium *Anabaena* sp. PCC 7120	Automated	10/10	Manual	10/10	
B.1	Yeast strain SK1	Automated	5/5	Manual	5/5	Rough milling of both samples performed in the same session.
B.2	Cyanobacterium *Anabaena* sp. PCC 7120	Automated	5/5	Automated	5/5	
C	Yeast strain SK1	Automated	20/20	Automated	11/20	Lamella were left in instrument for 10h before polishing, leading to lamellae bending and a lower success rate.
D	Cyanobacterium *Anabaena* sp. PCC 7120	Automated	7/7	Automated	7/7	
E	Cyanobacterium *Anabaena* sp. PCC 7120	Automated	7/7	Automated	7/7	
F	Cyanobacterium *Anabaena* sp. PCC 7120	Automated	18/19	Automated	16/18	User selected one target two times for rough milling, leading to failure in rough milling.
		Total Automated	72/73 (99%)	Total Automated	46/57 (81%)	

25

556
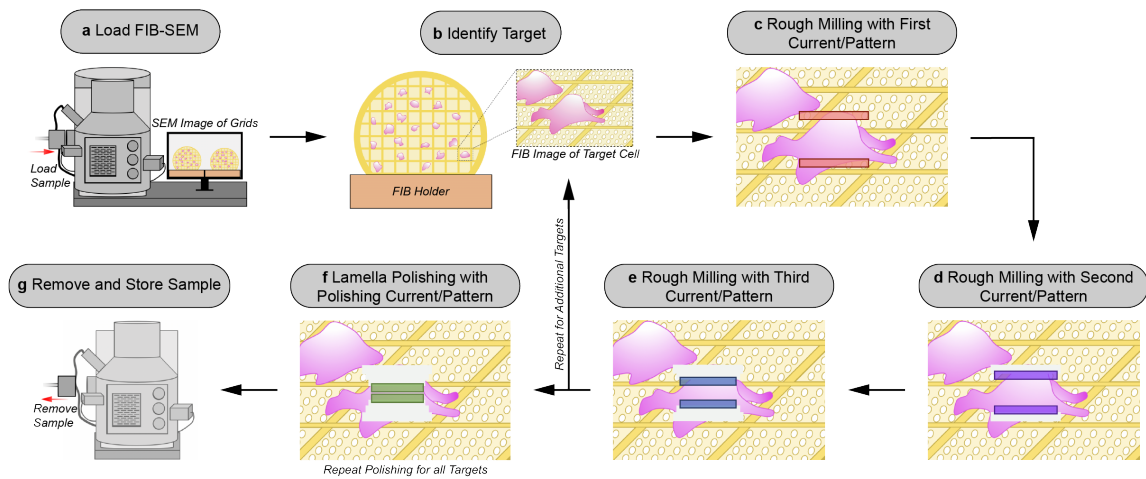
Supplementary Figure 1. Schematic of the manual cryoFIB milling workflow.

a: The sample is loaded into the FIB-SEM instrument.

b: A target is centered in the FIB image.

c-e: The first pair of rough milling patterns is placed on the target and milling is executed (c). Lamellae milling is observed via a live FIB view to determine when a milling step is completed. The same procedure is repeated for the second (d) and third (e) rough milling patterns. After rough milling of the target is completed, additional targets can be milled by repeating steps b-e.

f: Rough-milled lamellae are polished with a fourth set of milling patterns. Polishing is repeated for all rough-milled lamellae.
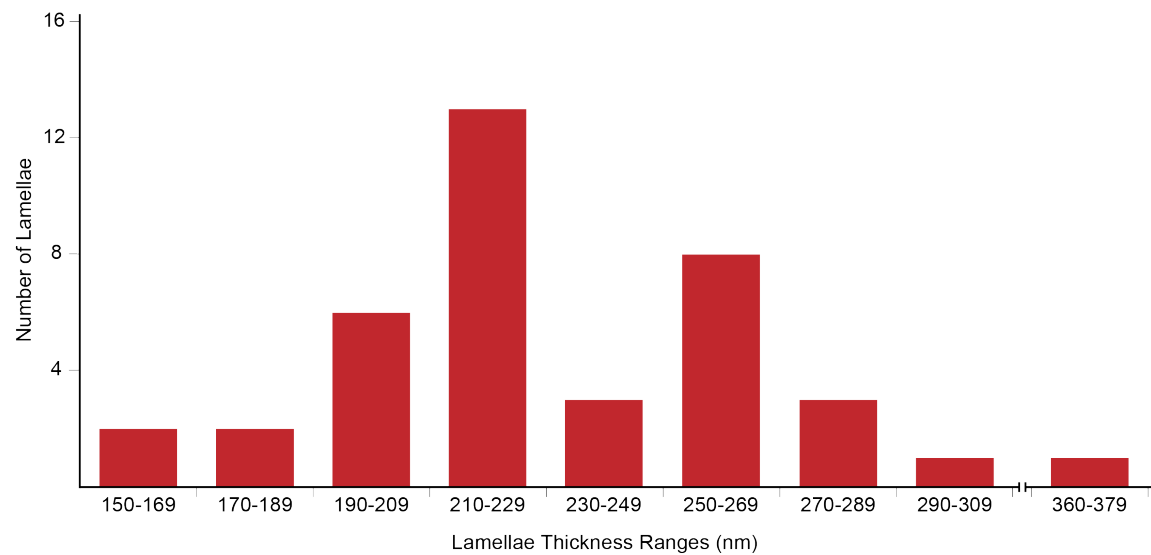
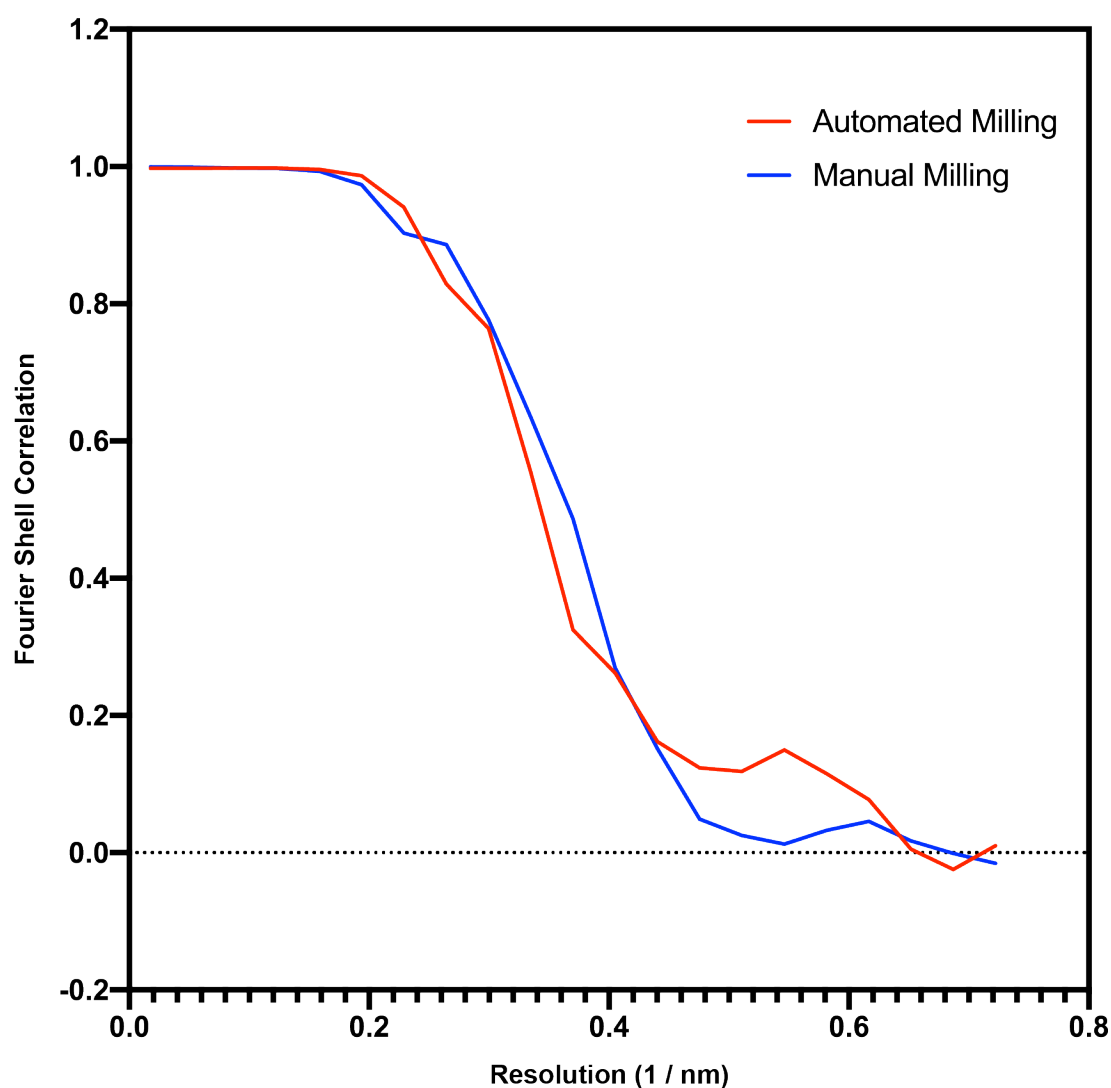**g:** The grids with milled lamellae are removed and stored.

572

Supplementary Figure 2. Distribution of lamellae thickness.

574 The plot shows the distribution of the thickness values of fully automated sequential
575 FIB-milled lamellae, as determined by cryoET imaging. The final polishing milling
576 patterns were spaced 300 nm apart.

577

578

Supplementary Figure 3. Comparison of data quality between manual and automated milling.

Shown is a Fourier Shell Correlation (FSC) curve (blue) for the septal junction subtomogram average shown in Figure 3i (resulting from automated milling). The second curve (red) results from a dataset published previously (Weiss et al., 2019) (resulting from manual milling) and was calculated with the same number of randomly selected subvolumes after 5-fold symmetrization (n=1715). Both approaches result in a comparable resolution estimate.

587

588

589

590 **Supplementary Table 1. Dimensions and currents used for each milling pattern**

591 **during automated sequential lamellae preparation.**

Milling Patterns 1 and 2 (Rough Milling 1)	30 kV 700 pA 9 x 5 μm rectange Patterns spaced 2 μm apart
Milling Patterns 3 and 4 (Rough Milling 2)	30 kV 300 pA 8 x 2 μm rectange Patterns spaced 1 μm apart
Milling Patterns 5 and 6 (Rough Milling 3)	30 kV 100 pA 7.5 x 1 μm rectange Patterns spaced 500 nm apart
Milling Patterns 7 and 8 (Lamella Polishing)	30 kV 50 pA 7 x 0.5 μm rectange Patterns spaced 300 nm apart
Drift Correction Pattern (Rough Milling and Polishing)	3 x 3 μm rectangle

592

593